



27 during the extension; (3) low velocities beneath the Moho that could represent either partially  
28 serpentinised mantle or mafic under-plating; and (4) a possible igneous composition of the PMR.

29

30 **Keywords:** Porcupine Basin, rifting, crustal thinning, seismic refraction

31

32 Rifted continental margins are important locations for oil and gas provinces, highlighted by the recent  
33 discoveries along the Atlantic conjugate margins and elsewhere (Mann *et al.* 2003; Levell *et al.*  
34 2010). The evaluation of the structure of sedimentary basins in such rifted margins, and the processes  
35 involved in their formation, are key to understanding the thermo-mechanical evolution of rifted  
36 margin systems. This understanding is essential in constraining, for example, regional stratigraphic  
37 development and time-temperature history of petroleum source rocks (e.g. White *et al.* 2003;  
38 Hantschel & Kauerauf 2009; Wangen 2010).

39 The Porcupine Basin, located west of Ireland, is an ideal natural laboratory to investigate these  
40 processes as the degree of crustal thinning varies dramatically from north to south (e.g. Tate *et al.*  
41 1993; Readman *et al.* 2005). Different parts of the basin may reflect and preserve evidence of  
42 different stages of continental rifting. The basin is underlain by thin to ultra-thin continental crust  
43 (O'Reilly *et al.* 2006) and is therefore an excellent location in which to investigate the processes  
44 associated with hyperextension (e.g. mantle serpentinisation; Reston *et al.* 2001).

45 The basin is lightly explored, with only 31 exploration and appraisal wells. There have been two oil  
46 and one gas condensate discoveries to date in the north of the basin (Naylor & Shannon 2011) and a  
47 number of other key wells, such as the recent Dunquin North 44/23-1 well, that confirmed the  
48 components of a working petroleum system in the centre of the basin (Wrigley *et al.* 2014). The  
49 recent increase in exploration interest, reflected in new Licensing Option awards, suggests that it will  
50 remain an active frontier exploration province in the coming years. However, unlocking the petroleum  
51 potential will require an improved understanding of basin structure and development (Wrigley *et al.*  
52 2014).

53 In this paper, we use wide-angle seismic data along two West-East lines that cross the Porcupine  
54 Basin axis, from the Porcupine Bank to the Irish Continental Shelf at 52.2°N and 51.4-51.5°N (Fig. 1),  
55 to provide an analysis of the crustal and uppermost mantle seismic velocities across the basin and  
56 briefly consider implications for its formation.

## 57 **GEOLOGICAL BACKGROUND**

58 The sedimentary record of the Porcupine Basin reveals a complex geodynamic and/or thermal history  
59 involving several episodes of rifting and subsidence that span from late Palaeozoic to late Mesozoic  
60 times, with the major rift phase occurring in Late Jurassic – Early Cretaceous times (Shannon 1991;  
61 Tate *et al.* 1993; Johnston *et al.* 2001; Naylor & Shannon 2011).

62 Based on subsidence analysis from available seismic reflection and well data, and using a simple Airy  
63 isostatic approach, Tate *et al.* (1993) estimated that lithospheric stretching factors increase from less  
64 than 2 in the north to more than 6 in the south of the Porcupine Basin (Fig. 1). Crustal thicknesses in  
65 Porcupine Basin have been estimated by 3D gravity modelling, with minimum thicknesses in the  
66 centre of the basin as low as 5 km (Welford *et al.* 2012). Recent results from wide-angle seismic data  
67 (O'Reilly *et al.*; 2006) suggest that the crust is even thinner in places and may be absent in the central  
68 part of the basin, over the Porcupine Arch (Fig. 1c). This observation may imply that the basin has  
69 experienced a more complex stretching history resulting in greater thinning, at least locally in the  
70 centre of the basin, than estimated by Tate *et al.* (1993).

71 Tate *et al.* (1993) also described a ridge feature, the Porcupine Median Ridge (hereafter, the PMR), in  
72 the middle of the southernmost part of the basin (Fig. 1). This feature was described further by Naylor  
73 *et al.* (1999, 2002). During the last three decades, this ridge has been successively interpreted as (1) a  
74 volcanic structure (e.g. Tate & Dobson 1988; White *et al.* 1992; Calvès *et al.* 2012); (2) a serpentinite  
75 mud diapir (Reston *et al.*, 2001, 2004); or (3) a block of continental crust (e.g., O'Sullivan *et al.* 2010;  
76 Hardy *et al.* 2010). Its nature is still debated.

77 Another striking feature is observed in the free-air gravity data: the Porcupine Arch (Fig. 1c), first  
78 described and named by Naylor *et al.* (2002). This feature appears as a gravity high and has been  
79 interpreted as the result of a very thin crust overlying partially serpentinised uppermost mantle

80 (Readman *et al.* 2005; O'Reilly *et al.* 2006). In contrast, the PMR is not evident in the gravity data  
81 (Fig. 1c). Readman *et al.* (2005) attributed the rapid variation of the gravity anomaly at the south of  
82 the Porcupine Arch to the presence of a major change of crustal thickness resulting from a transfer  
83 zone, involving different tectonic regimes in the northern and southern Porcupine Basin.

## 84 **DATA AND METHOD**

### 85 **The data acquisition and seismic phases**

86 The data used in this study were acquired during an offshore/onshore wide-angle-seismic experiment  
87 that was completed by GEOMAR and DIAS in May 2004.

#### 88 *The northern profile*

89 The northern profile is a 270 km shot line running across the Porcupine Basin, from West to East, at  
90 52.2°N. Here, 2258 shots were recorded by 22 sea-bottom instruments (Fig. 1c): ten ocean bottom  
91 hydrophones (OBH) and twelve ocean bottom seismometers (OBS). Data are of generally good  
92 quality (Figs. 2a and 2c), allowing the identification of seismic arrivals to up to 110 km distance  
93 between the source and the receiver. A thorough study of the seismograms allowed for the  
94 identification of thirteen seismic phases: the arrivals of refractions turning in seven different layers  
95 and wide-angle reflections at the corresponding six geological interfaces. The four shallowest layers  
96 are observed on most instruments of the central part of the basin. They correspond to sedimentary  
97 layers and show apparent velocities of 1.5-1.6 km/s, 2 km/s, 2.75 km/s and 3.75 km/s, from top to  
98 bottom. The refracted arrivals of the three deeper layers are observed at further offsets, with apparent  
99 velocities of 5-5.5 km/s, 6-6.5 km/s and 7.5-8 km/s, which are typical for two crustal layers and the  
100 upper mantle, respectively.

#### 101 *The southern profile*

102 A total of 31 ocean-bottom instruments were deployed along the 307-km-long southern line. First, ten  
103 OBH and fifteen OBS were deployed every ~8 km along a 2D line and recorded 2523 shots:  
104 instruments 1 to 25 (Fig. 1c). However, OBH 05 and 24 failed to record useable data and a second  
105 seismic survey taking place in the study area at the same time made the easternmost part of the line

106 very noisy. For this reason, part of the line was re-shot later. Then, six ocean-bottom instruments were  
107 deployed and 702 shots were recorded by instruments 90 to 95 (Fig. 1c). The location of the  
108 instruments was chosen to increase the data density above the Porcupine Median Ridge, reducing the  
109 instrument spacing along this profile down to 4 km in the central part of the line. Apart from the  
110 easternmost part of the first shot line, the data are of very good quality (Figs. 2e and 2g), showing  
111 good arrivals to source-receiver distances of 80-120 km on most instruments. The seismograms allow  
112 the identification of eleven seismic phases: six refractions and five wide-angle reflections. Three  
113 sedimentary layers were identified, with apparent velocities of 2.5 km/s, 3.25 km/s and 5-5.25 km/s,  
114 from top to bottom. The third sedimentary refracted phase corresponds to arrivals of rays turning in  
115 the lowermost sediments and the PMR. As for the northern profile, arrivals from the three deeper  
116 layers corresponded to two crustal layers and the upper mantle. These arrivals had apparent velocities  
117 of 5.5-6 km/s, 6.5-7 km/s and 7-8 km/s, respectively.

### 118 **Data processing and picking**

119 The phases identified on each seismogram were picked manually. In total, 31,676 and 62,977 arrivals  
120 were picked along the northern and southern profiles, respectively (Tables 1 and 2).

121 Data were picked on unprocessed seismograms first, using both hydrophone and vertical geophone,  
122 where available. Further arrivals were picked using deconvolved and filtered seismograms. These  
123 later picks were done with care to avoid introducing a time shift in the picking. Deconvolution was  
124 done in 2 steps: (1) spiking deconvolution, and (2) predictive deconvolution, with a gap length of  
125 0.386 s. Then, a band-pass filter was applied, with corner frequencies of 1-5-15-25 Hz. Processed data  
126 were also used for display (Fig. 2). This processing significantly improved the signal-to-noise ratio  
127 and allowed for the retrieval of signal at far offsets, up to source-receiver distances of 100-120 km.

128 Some instruments show a high velocity set of arrivals at source-receiver distances of 5-20 km (e.g.  
129 black arrows on Fig. 2h). These arrivals correspond to a 5-5.25 km/s layer in the sediments that is  
130 probably thin (up to a few hundred meters) and would be poorly resolved by travel-time tomography.  
131 Thus, we ignored these arrivals in this study.

132 Picking uncertainties were set using the signal to noise ratio of the data trace 250 ms before and after  
133 the picked arrival for each arrival time, following [Zelt & Forsyth's \(1994\)](#) empirical relationship, and  
134 an offset dependent relationship for offsets < 40 km. Thus, picking uncertainties vary from 20 to 125  
135 ms.

### 136 **Modelling strategy**

137 Picks from both lines were modelled using the Tomo2D code ([Korenaga \*et al.\* 2000](#)). This  
138 tomography method solves the forward problem by first obtaining the residual travel times by means  
139 of ray-tracing and then solving a linearised inverse problem to reduce the residuals. Since the initial  
140 model is always far from the solution, the linearised inverse problem has to be solved iteratively. To  
141 prevent excessive model perturbation, the method includes some regularisation represented by  
142 velocity and depth smoothing (parameterised by correlation lengths) and damping constraints to  
143 stabilise the iterative inversion.

144 The picked phases were inverted following a layer stripping strategy ([Sallarès \*et al.\* 2011](#)) to allow for  
145 imaging wide-angle reflections together with the corresponding refracted phases. Thus, we proceeded  
146 by building the model layer by layer, resolving at each step the velocity and depth structure of a layer,  
147 from top to bottom.

148 For each step, starting velocity models were built using the apparent velocities observed on the  
149 seismograms together with the velocities and reflector depth from the previous layer. Moho depth  
150 beneath the Irish Continental Shelf, southwest of Ireland, was constrained using the results of an  
151 onshore refraction study ([O'Reilly \*et al.\* 2010](#)).

152 The velocity models of the Northern and Southern profiles were built in seven and six steps,  
153 respectively ([Figs. 3a and 3b](#)). At each step, the resulting models reproduce well the picks within their  
154 uncertainties ( $\chi^2$  values lower than 1, [Tables 1 and 2](#)). An indication of the density of the ray coverage  
155 in the final models is provided by the derivative weight sum (DWS, [Figs. 3c and 3d](#)). The DWS gives  
156 an indication of which areas of the models are better resolved. The central and shallow areas of the  
157 models have the densest ray coverage. Thus, this is where we can expect the best resolution and  
158 reliability of results.

## 159 VELOCITY MODELS

160 The velocity models show the geometry of the sedimentary basin, the thinning of the crust and the  
161 velocity structure in the uppermost mantle (Fig. 3a and 3b).

### 162 Northern line

163 The tomography model of the northern profile shows the P-wave velocity structure in the sediments,  
164 crust and upper mantle together with the geometry of the six reflectors: four in the sediments, one in  
165 the basement and the Moho (Fig. 3a).

166 The velocity structure from the seafloor down to the deepest sedimentary reflection shows velocities  
167 ranging from 1.6 to ~3.5 km/s (Fig. 4a). These velocities are characteristic of post-rift sediments  
168 (Cenozoic to Cretaceous) according to previous refraction studies in the area (O'Reilly *et al.* 2006).

169 Also, the lateral continuity of these layers indicates no significant evidence of disruption or  
170 deformation that could be attributed to the effects of active fault-controlled rifting. Below these, no  
171 wide-angle reflectivity from the syn-rift and pre-rift sections is identified on the record sections, and  
172 thus, no interface bounding these layers is retrieved in this model. However, velocities of 4-5 km/s  
173 might correspond to isolated syn-rift packages rotated by normal faults, e.g. at 90 km model distance  
174 and 7 km depth (Fig. 3a). Below these packages, an intra-basement reflector is defined across the  
175 basin, showing a velocity contrast from 5 to 5.5 km/s in some regions. The velocities observed in this  
176 layer might represent either pre-rift sediments or fractured crystalline crust. Below this intra-basement  
177 reflector, seismic velocities increase downwards from 5.5-6 to 6.8-6.9 km/s at the Moho discontinuity  
178 (Fig. 4a), which shows major asymmetry across the basin. The lowermost basement shows velocities  
179 up to 6.8-6.9 km/s where the crust is thick and up to 6.5 km/s in the central part of the basin where the  
180 crust is highly thinned (km 100-130, see Fig. 4a). The model shows a strong velocity contrast, from  
181 6.5-7 to more than 7.5 km/s, at the Moho discontinuity. Seismic velocities range from 7.5 to ~8.1  
182 km/s in the uppermost mantle. Interestingly, we observe velocities as low as 7.4 km/s at model  
183 distances of 90 and 115 km in the uppermost mantle (Fig. 4a), coinciding with the progressive  
184 eastward thinning of the crust.

185 In summary, the northern profile features: (1) an 8-9 km thick post-rift sedimentary sequence, (2) an  
186 asymmetric crustal structure, and (3) crustal thinning from 30 km near the Irish coastline to less than 5  
187 km in the central part of the basin (km 120), using a velocity contour of 5 km/s for the top of the  
188 crystalline basement and the Moho reflection for the base of the crust.

### 189 **Southern line**

190 The tomography model for the southern profile shows the velocity structure in the sediments, crust  
191 and upper mantle together with the geometry of the five reflectors (Fig. 3b). The first two sedimentary  
192 layers show velocities of 1.65 to 3.0 km/s and 3.0 to 3.5 km/s, respectively (Fig. 4b). The third layer  
193 corresponds to the deepest sedimentary layer together with the PMR. This third layer shows higher  
194 velocities, reaching 6 km/s in the middle of the basin, at model distances of 155 to 185 km,  
195 corresponding to the location of the PMR (Fig. 4b). These velocities are consistent with a volcanic  
196 origin but do not exclude other interpretations. On the eastern side of the PMR, velocities are typical  
197 for compacted sediments. There is little velocity contrast between the PMR and surrounding  
198 sediments, and reflections from the top of the PMR are few. Thus, for our modelling, we decided to  
199 model the ridge and adjacent sub-basins as a single layer. We modelled high velocities on the western  
200 side of the ridge, with values of 5 to 5.2 km/s at model distances of 140 to 160 km and depths of 6-7  
201 km. These velocities would also be consistent with a volcanic origin. These high velocities are  
202 observed near the top of the PMR. Beneath this layer, we modelled the basement as two layers. The  
203 upper basement generally shows velocities of 5-5.5 to 6 km/s. The velocities of 5-5.5 km/s might  
204 correspond to compacted pre-rift sediments or highly fractured crystalline basement. The lower  
205 basement shows velocities of 6-7 km/s (Fig. 4b). The velocity contrast between upper and lower  
206 basement is most obvious in the centre of the basin, at model distances of 120 to 200 km. Uppermost  
207 mantle velocities range from 7 km/s beneath the western part of the basin to 7.5 km/s in the centre, at  
208 a model distance of 160 km, just beneath the PMR, and decrease slightly to the East, with a velocity  
209 of 7.3 km/s just beneath the Moho (Fig. 4b). However, the velocities of 7 km/s beneath the western  
210 part of the basin are poorly resolved as this area is covered by few rays, all propagating eastward (Fig.  
211 3d).



212 Thus, the southern profile features: (1) a 7 km thick post-rift sedimentary sequence with velocities up  
213 to 4-4.5 km/s, (2) a high velocity area in the central part of the basin, corresponding to the PMR, and  
214 an adjacent high velocity layer, showing seismic velocities consistent with a volcanic origin, (3)  
215 asymmetric crustal thinning compatible with a component of simple shear along a detachment surface  
216 during the extension, (4) a wide zone of highly thinned crust, where the crust is 6 km thick or less  
217 over a 90 km wide area, and could be as thin as 3 km at km 150, and (5) an uppermost mantle with  
218 velocities of 7.3 to 7.5 km/s just below the Moho.

## 219 **COMPARISON WITH BOREHOLE AND REFLECTION DATA**

### 220 **Comparison of modelled velocities with well log data**

221 Comparison of borehole seismic velocity measurements with our models can aid interpretation, and is  
222 also a way to validate our model. Sonic velocities compare well with the two models, generally  
223 differing by less than 100-200 m/s (Fig. 5). Velocities from wide-angle data show smoother variations  
224 than the well data, due to the method: seismic travel-times give an average of the velocities in the  
225 subsurface, with lower resolution than well-log data. Note that tomography models produced by the  
226 layer-stripping method allow changes in the velocity gradient at interfaces but not abrupt velocity  
227 jumps.

228 Well 35/21-1, which terminated in Eocene strata, is located 5.4 km north of the northern line near a  
229 model distance of 114.7 km (Fig. 5a). Comparison of the velocity-depth profile of the well with our  
230 tomography model at the projected position of the well along the northern profile shows a good  
231 correlation of the overall velocities down to the bottom of the well.

232 Well 43/13-1, which terminated in Upper-Jurassic strata, is located approximately 7 km north of the  
233 southern line near a model distance of 110.5 km (Fig. 5b). The well data and tomography results  
234 along the southern line also show a very good correlation of the velocities at depth.

235 The velocity differences observed between the well log data and the velocity models probably arise  
236 because the wells are not located exactly on the velocity profiles and sediment velocities can vary  
237 laterally by 100-500 m/s (Fig. 4b).

## 238 **Comparison of the models with coincident seismic reflection profiles**

239 Combining the velocity models with coincident seismic reflection data allows a comparison between  
240 the two images, thereby helping to improve interpretation of the seismic reflection data at depth (Figs.  
241 6 and 7). A Kirchhoff pre-stack depth migration was applied to the seismic reflection data, using  
242 velocities from residual move-out and depth focusing analysis in a top down approach. The image  
243 output from this method is sharper than the image output using velocities from wide-angle  
244 tomography. The RMS differences between velocities from the wide-angle data and velocities used  
245 for pre-stack depth migration in the basin area are 0.022 and 0.026 km/s for the northern and southern  
246 lines, respectively. There is a remarkable correspondence between the independently-derived velocity  
247 models and the coincident seismic reflection profiles.

### 248 *Northern line*

249 The seismic reflection profile Wire 2 (Croker & Klempere 1989) is coincident with the northern  
250 profile. We compared the velocity structure of the basin with the tectonic structure observed in a pre-  
251 stack depth migration of Wire 2 (Fig. 6). Figure 6c shows that the post-rift sedimentary cover has  
252 velocities ranging from 1.6 to ~4.0-4.5 km/s. Below this sedimentary package, velocities between 4.5  
253 and 5 km/s overlie rotated syn-tectonic sediments, while velocities between 5 and 6.9 km/s are mainly  
254 representative of the crystalline basement, though velocities between 5 and 5.5 km/s might also  
255 represent pre-rift sediments. The base of the half-graben structure observed in the middle of the basin  
256 (i.e. 120-125 km model distance and 8 km depth, Fig. 6b) is well defined by seismic velocities of 5  
257 km/s that coincide with the crystalline basement. The top of the mantle from the seismic velocity  
258 model (Fig. 6c) coincides with high amplitude reflections at 14 km depth and CDP 5700-6500 on  
259 profile Wire 2 (Fig. 6b). Thus, these reflections observed on Wire 2 might also correspond to the  
260 crust-mantle boundary.

### 261 *Southern line*

262 The superposition of the velocity model of the southern line with the coincident SPB97-115 seismic  
263 reflection profile (Reston *et al.* 2001, 2004) allows us to compare the velocities with the reflectivity  
264 (Fig. 7). Velocities from 1.6 to ~5 km/s follow the sedimentary structures. In particular, velocities

265 between 4 and 5 km/s highlight typical syn-rift deposits, i.e. tilted-blocks like those observed along  
266 the northern line, at models distances of 105-125 km (Fig. 7c). The PMR, located between CDP 4500  
267 and 6500 at 5 to 9 km depth (Fig 7b), shows velocities from 4.7 km/s at its top to 6 km/s at its base,  
268 which are higher than the surrounding sediments. Also, a set of reflectors with higher amplitude than  
269 the sediments above and below, is observed in the western part of the basin, at CDP 3000 to 5000, at  
270 depths of 5.5 to 7 km (Fig. 7a). These reflectors are coincident with a high velocity layer in the  
271 sedimentary sequence, with velocities of 5-5.25 km/s. Also, velocities in the eastern part of the basin,  
272 east of the PMR, are generally lower than those in the western part of the basin. The SPB97-115  
273 profile shows some deep reflectivity at approximately 14 km depth, CDP 5500-7000 (Fig. 7b). This  
274 reflectivity is coincident with the top of the mantle of the velocity model at km 175-190, where  
275 seismic velocities jump from ~6.5 to 7.3 km/s (Fig. 7c). Thus, this deep reflectivity corresponds to the  
276 Moho discontinuity.

## 277 **DISCUSSION**

278 The highly stretched region of Porcupine Basin widens slightly towards the south, from  
279 approximately 100 km along the northern profile to 115 km along the southern profile. The width of  
280 the region of highly stretched crust, with crustal thicknesses < 6 km, is about 90 km along the  
281 southern profile and less than 30 km along the northern profile. These two observations show the  
282 extent to which the basin is more stretched in the south than in the north (Figs. 3a and 3b). Also, the  
283 crustal structures across both lines are asymmetric, including, in particular, the morphology of the  
284 Moho discontinuity. Such asymmetry is compatible with a model in which some of the crustal  
285 deformation has been accommodated by simple shear along a crustal discontinuity during rifting.  
286 Reston *et al.* (2001) proposed that the rifting in Porcupine Basin changed from a symmetric to an  
287 asymmetric mode as upper mantle serpentinisation began as a result of the embrittlement of the crust.  
288 Such asymmetry is shown also by numerical models (e.g. Brune *et al.* 2014; Huisman & Beaumont  
289 2014) and conceptual models built from geological observations in the Alps and West Iberia (e.g.  
290 Manatschal 2004).

291 We calculated maximum stretching factors as the ratio between the assumed pre-rift crustal thickness  
292 (30 km; [Lowe & Jacob 1989](#); [O'Reilly et al. 2010](#)) and the minimum thicknesses of the crystalline  
293 basement, 5 and 3 km along the northern and southern lines, respectively. Thus, the maximum crustal  
294 stretching factors increase from 6 along the northern line to 10 along the southern line. Greater crustal  
295 thicknesses, up to 34 km, have been estimated from a receiver function study beneath southern Ireland  
296 ([Licciardi et al. 2014](#)), so stretching factors may reach even higher values. These values are much  
297 greater than the lithospheric stretching factors previously estimated from subsidence ([Fig. 1](#); [Tate et](#)  
298 [al. 1993](#)). The maximum lithospheric stretching factors inferred by [Tate et al. \(1993\)](#) are only ~2.5  
299 along the northern profile and 5 along the southern profile, which is half or less of the crustal  
300 stretching factors obtained in this study. The lithospheric stretching factors were estimated by a  
301 subsidence analysis that assumed pure shear extension, made a variety of simplistic assumptions, and  
302 used a limited amount of older seismic reflection and well data.

303 The high crustal stretching factors, 6 and 10, imply that the crust became entirely brittle during the  
304 rifting, allowing crustal-scale faults to reach the mantle and the sea water to percolate through these  
305 faults and serpentinise the uppermost mantle ([O'Reilly et al. 1996](#); [Pérez-Gussinyé & Reston 2001](#)).  
306 This process is compatible with the low velocities observed in the uppermost mantle, which are 7.4-  
307 7.8 km/s along the northern line and only 7.3-7.5 km/s along the southern line. Thus, the mantle  
308 velocities decrease significantly from north to south. The observed mantle velocities can be explained  
309 by 8 to 20 % serpentinisation along the northern line and approximately 20 % along the southern line  
310 ([Carlson & Miller 2003](#)). Such velocities are also compatible with the presence of mafic intrusions in  
311 the uppermost mantle (e.g. [Funck et al. 2008](#)). The difference between crustal and inferred  
312 lithospheric stretching factors may be attributed to a combination of (1) bias in the lithospheric  
313 stretching estimates due to the simplifying assumptions, (2) mantle serpentinisation ([O'Reilly et al.](#)  
314 [1996](#)) beneath the thin crust and/or addition of material at the base of the crust, (3) real differences in  
315 stretching factors between the crust and mantle lithosphere, and (4) dynamic topography resulting  
316 from the Iceland plume activity ([Hartley et al. 2011](#)).

317 Along the southern profile, a basement high corresponds to the PMR, where velocities range from 4.7  
318 to 6 km/s. Similar velocities are observed west of the PMR, overlying high reflectivity in the

319 sedimentary succession (Fig. 7). The seismic velocity of both the PMR and the intra-sedimentary  
320 layer is consistent with that of volcanic rocks (e.g. Christensen 1982; Eldholm & Grue 1994). Thus,  
321 using both refraction and reflection seismic imaging, we interpret the PMR as a volcanic feature. The  
322 velocities in the PMR are slower than might be expected for a serpentinite diapir, reaching values as  
323 low as 4.7 km/s. Velocities are also lower than those expected for continental crustal rocks and, based  
324 on this observation and the morphology of the ridge, we do not favour the tilted-block hypothesis. At  
325 this stage we cannot exclude the serpentinite diapir and tilted-block hypotheses: serpentinite could be  
326 mixed with sediments and a tilted crustal block could be highly fractured, also decreasing the  
327 velocities. Nevertheless, the geometry and seismic velocities of the PMR favour a volcanic structure.  
328 High seismic velocities similar to the PMR velocities and a velocity inversion in the underlying  
329 sediments also favour an igneous nature (e.g. intrusive sills or volcanic flows) of the highly reflective  
330 intra-sedimentary layer. If these volcanics were related to the PMR, their presence would imply that  
331 the PMR had at least two main phases of activity: (1) a first phase during which the volcanic ridge  
332 formed, sitting near the base of the post-rift sediments, and (2) a more recent phase, with volcanic  
333 flows or sills emplaced during the post-rift sedimentation of the basin. Similar poly-phase magmatic  
334 activity has been observed in volcanic islands such as the Canary Islands (e.g. Ancochea *et al.* 2006).  
335 Although a detailed analysis of the thermal evolution of the basin is beyond the scope of the present  
336 study, it is worth noting that our results have implications for the amount and timing of heat affecting  
337 the sediments, and thus the thermal maturity of Mesozoic source rocks. For example, Naeth *et al.*  
338 (2005) used the lithospheric stretching factors (Fig. 1; Tate *et al.* 1993) to estimate the thermal history  
339 of the basin, but assumed uniform stretching based upon McKenzie's (1978) model. Our inferred  
340 crustal stretching factors are larger than the lithospheric stretching factors inferred by Tate *et al.*  
341 (1993). New thermal models are needed to estimate the influence of higher stretching factors on the  
342 heat-flow. In addition to the amount and nature of stretching and extensional strain rates, the presence  
343 of volcanism of various ages and of serpentinitised upper mantle in this area provide additional  
344 components to the complex thermal history as well as the tectono-sedimentary evolution of the basin.

## 345 **CONCLUSIONS**

346 In this study, we determined the crustal and upper mantle structure across Porcupine Basin, from the  
347 Porcupine Bank to the Irish shelf, along two east-west profiles, 90 km apart from each other. We  
348 conclude that:

- 349 • The large-scale crustal structure is highly asymmetric, which is compatible with a component  
350 of simple shear during crustal stretching. Crustal thinning increases from north to south in the  
351 basin. The continental crust is highly stretched along the whole basin, with maximum crustal  
352 stretching factors increasing toward the south, from 6 to 10 between the two profiles. Also,  
353 the highly thinned crust occurs across a wider area in the south (90 km) than in the north (<  
354 30 km).
- 355 • The PMR shows seismic velocities that are consistent with volcanics but do not exclude other  
356 interpretations. The PMR is located just east of a high-velocity / highly reflective layer in the  
357 sediment column, which we interpret as of igneous origin. The relationship between this  
358 feature and the PMR is unclear.
- 359 • Seismic velocities in the upper mantle are lower than those of typical unaltered peridotites,  
360 indicating the presence of either partially serpentinised mantle (10-20%, degrees of  
361 serpentinisation increasing toward the south) or mafic intrusions beneath the base of the crust,  
362 in particular in the southern part of the basin.

## 363 **ACKNOWLEDGMENTS**

364 This project is funded by the Irish Shelf Petroleum Studies Group (ISPSG) of the Irish Petroleum  
365 Infrastructure Programme Group 4. The ISPSG comprises: Atlantic Petroleum (Ireland) Ltd, Cairn  
366 Energy Plc, Chrysaor E&P Ireland Ltd, Chevron North Sea Limited, ENI Ireland BV, Europa Oil &  
367 Gas (Holdings) plc, ExxonMobil E&P Ireland (Offshore) Ltd., Kosmos Energy LLC, Maersk Oil  
368 North Sea UK Ltd, Petroleum Affairs Division of the Department of Communications, Energy and  
369 Natural Resources, Providence Resources plc, Repsol Exploración SA, San Leon Energy Plc, Serica  
370 Energy Plc, Shell E&P Ireland Ltd, Sosina Exploration Ltd, Statoil (UK) Ltd, Tullow Oil Plc and  
371 Woodside Energy (Ireland) Pty Ltd. Gravity, seismic and well data were provided by the Petroleum

372 Affairs Division of the Department of Communications, Energy & Natural Resources, Ireland.  
373 Seismic reflection data along profile SPB97-115 were supplied by Fugro-Geoteam through Conoco-  
374 Phillips. Profile Wire2 was acquired during the BIRPS WIRE project, which was funded by the  
375 Natural Environment Research Council (UK), the Department of Energy (Ireland) and Western  
376 Geophysical. We thank K. Welford and an anonymous reviewer for their constructive comments and  
377 suggestions. GMT was used to prepare all the figures (Wessel & Smith 1998) and was combined with  
378 Seismic-Unix (Stockwell 1999) for Figures 2, 6 and 7. Minshull was supported by a Wolfson  
379 Research Merit award.

## 380 REFERENCES

381 Ancochea, E., Hernán, F., Huertas, M. J., Brändle, J. L. & Herrera, R. 2006. A new  
382 chronostratigraphical and evolutionary model for La Gomera: implications for the overall evolution of  
383 the Canarian Archipelago. *Journal of Volcanology and Geothermal Research*, **157**(4), 271-293,  
384 doi:10.1016/j.jvolgeores.2006.04.001.

385 Brune, S., Heine, C., Pérez-Gussinyé, M. and Sobolev, S.V. 2014. Rift migration explains  
386 continental margin asymmetry and crustal hyper-extension. *Nature Communications*, **5**,  
387 doi:10.1038/ncomms5014

388 Calvès, G., Torvela, T., Huuse, M. & Dinkleman, M. G. 2012. New evidence for the origin of  
389 the Porcupine Median Volcanic Ridge: Early Cretaceous volcanism in the Porcupine Basin, Atlantic  
390 margin of Ireland. *Geochemistry, Geophysics, Geosystems*, **13**(6), doi:10.1029/2011GC003852.

391 Carlson, R. L. & Miller, D. J. 2003. Mantle wedge water contents estimated from seismic  
392 velocities in partially serpentized peridotites. *Geophysical Research Letters*, **30**(5),  
393 doi:10.1029/2002GL016600.

394 Christensen, N. I. 1982. Seismic velocities, In: *Handbook of physical properties of rocks*, **2**,  
395 1-228.

396 Croker, P. F. & Klemperer, S. L. 1989. Structure and Stratigraphy of the Porcupine Basin:  
397 Relationships to Deep Crustal Structure and the Opening of the North Atlantic, in *Extensional*

398 *Tectonics and Stratigraphy of the North Atlantic Margins*, eds Tankard A.J., Balkwill H.R., *American*  
399 *Association of Petroleum Geologists*, Tulsa, **46**, 445-159.

400 Eldholm, O. & Grue, K. 1994. North Atlantic volcanic margins: Dimensions and production  
401 rates, *Journal of Geophysical Research*, **99**(B2), 2955-2968, doi:10.1029/93JB02879.

402 Funck, T., Andersen, M. S., Keser Neish, J. & Dahl-Jensen, T. 2008. A refraction seismic  
403 transect from the Faroe Islands to the Hatton-Rockall Basin. *Journal of Geophysical Research - Solid*  
404 *Earth*, **113**(B12), doi:10.1029/2008JB005675.

405 Hantschel, T. and Kauerauf, A.I. 2009. *Fundamentals of basin and petroleum systems*  
406 *modeling*. Springer Science & Business Media.

407 Hardy, R.J.J., Querendez, E., Biancotto, F., Jones, S.M., O'Sullivan, J. & White, N. 2010.  
408 New methods of improving seismic data to aid understanding of passive margin evolution: a series of  
409 case histories from offshore west of Ireland. In *Geological Society, London, Petroleum Geology*  
410 *Conference series*, **7**, 1005-1012, doi:10.1144/0071005.

411 Hartley, R.A., Roberts, G.G., White, N. and Richardson, C. 2011. Transient convective uplift  
412 of an ancient buried landscape. *Nature Geoscience*, **4**(8), 562-565, doi:10.1038/ngeo1191.

413 Huisman, R.S. and Beaumont, C. 2014. Rifted continental margins: the case for depth-  
414 dependent extension. *Earth and Planetary Science Letters*, **407**, 148-162,  
415 doi:10.1016/j.epsl.2014.09.032.

416 Johnston, S., Doré, A. G. & Spencer, A. M. 2001. The Mesozoic evolution of the southern  
417 North Atlantic region and its relationship to basin development in the south Porcupine Basin, offshore  
418 Ireland. *Geological Society, London, Special Publications*, **188**(1), 237-263,  
419 doi:10.1144/GSL.SP.2001.188.01.14.

420 Korenaga, J., Holbrook, W. S., Kent, G. M., Kelemen, P. B., Detrick, R. S., Larsen, H. C.,  
421 Hopper, J. R. & Dahl-Jensen, T. 2000. Crustal structure of the southeast Greenland margin from joint  
422 refraction and reflection seismic tomography. *Journal of Geophysical Research - Solid Earth*, **105**,  
423 21591-21614, doi:10.1029/2000JB900188.



424 Levell, B., Argent, J., Doré, A. G., & Fraser, S. 2010. Passive margins: overview. In  
425 *Geological Society, London, Petroleum Geology Conference series 7*. Geological Society of London,  
426 823-830.

427 Licciardi, A., Agostinetti, N. P., Lebedev, S., Schaeffer, A. J., Readman, P.W. & Horan, C.  
428 2014. Moho depth and Vp/Vs in Ireland from teleseismic receiver functions analysis. *Geophysical*  
429 *Journal International*, **199**, 561-579, doi:10.1093/gji/ggu277.

430 Lowe, C. & Jacob, A.W.B. 1989. A north–south seismic profile across the Caledonian suture  
431 zone in Ireland. *Tectonophysics*, **168**(4), 297-318, doi:10.1016/0040-1951(89)90224-2.

432 Manatschal, G. 2004. New models for evolution of magma-poor rifted margins based on a  
433 review of data and concepts from West Iberia and the Alps. *International Journal of Earth Sciences*,  
434 **93**(3), 432-466, doi:10.1007/s00531-004-0394-7.

435 Mann, P., Gahagan, L., & Gordon, M. B. 2003. Tectonic setting of the world's giant oil and  
436 gas fields. In *M. T. Halbouty, ed., Giant oil and gas fields of the decade 1990–1999*, AAPG Memoir  
437 **78**, 15-105.

438 McKenzie, D.P. 1978. Some remarks on the development of sedimentary basins. *Earth &*  
439 *Planetary Science Letters*, **40**, 25-32, doi:10.1016/0012-821X(78)90071-7.

440 Naylor, D. & Shannon, P.M. 2011. *Petroleum Geology of Ireland*. Dunedin Academic Press,  
441 Edinburgh, Scotland. 262 pages.

442 Naylor, D., Shannon, P. & Murphy, N. 1999. *Irish Rockall region – a standard structural*  
443 *nomenclature system*. Petroleum Affairs Division. Special Publication 1/99. 42 pages and 2  
444 Enclosures.

445 Naylor, D., Shannon, P. & Murphy, N. 2002. *Porcupine-Goban region – a standard*  
446 *structural nomenclature system*. Petroleum Affairs Division. Special Publication 1/02. 65 pages and 2  
447 Enclosures.

448 Naeth, J., Di Primio, R., Horsfield, B., Schaefer, R. G., Shannon, P. M., Bailey, W. R., &  
449 Henriot, J. P. 2005. Hydrocarbon seepage and carbonate mound formation: a basin modelling study  
450 from the Porcupine Basin (offshore Ireland). *Journal of Petroleum Geology*, **28**(2), 147-166,  
451 doi:10.1111/j.1747-5457.2005.tb00077.x.

452 O'Reilly, B.M., Hauser, F., Jacob, A.W.B. & Shannon, P.M. 1996. The lithosphere below the  
453 Rockall Trough: wide-angle seismic evidence for extensive serpentinisation. *Tectonophysics*, **255**, 1-  
454 23, doi:10.1016/0040-1951(95)00149-2.

455 O'Reilly, B. M., Hauser, F., Ravaut, C., Shannon, P. M. & Readman, P. W. 2006. Crustal  
456 thinning, mantle exhumation and serpentinization in the Porcupine Basin, offshore Ireland: evidence  
457 from wide-angle seismic data. *Journal of the Geological Society, London*, **163**, 775-787,  
458 doi:10.1144/0016-76492005-079.

459 O'Reilly, B. M., Hauser, F. & Readman, P. W. 2010. The fine-scale structure of upper  
460 continental lithosphere from seismic waveform methods: insights into Phanerozoic crustal formation  
461 processes. *Geophysical Journal International*, **180**(1), 101-124, doi:10.1111/j.1365-  
462 246X.2009.04420.x.

463 O'Sullivan, J. M., Jones, S. M. & Hardy, R. J. 2010. Comparative analysis of the Porcupine  
464 Median Volcanic Ridge with modern day Pacific Ocean seamounts—further evidence of an amagmatic  
465 Mesozoic basin history for the South Porcupine Basin, offshore Ireland. *Conjugate Margins  
466 Conference 2010*, **5**, 216-219.

467 Pérez-Gussinyé, M. & Reston, T. J. 2001. Rheological evolution during extension at  
468 nonvolcanic rifted margins: onset of serpentinization and development of detachments leading to  
469 continental breakup. *Journal of Geophysical Research - Solid Earth*, **106**(B3), 3961-3975,  
470 doi:10.1029/2000JB900325.

471 Readman, P. W., O'Reilly, B. M., Shannon, P. M. & Naylor, D. 2005. The deep structure of  
472 the Porcupine Basin, offshore Ireland, from gravity and magnetic studies. In *Geological Society,  
473 London, Petroleum Geology Conference series*, **6**, 1047-1056, doi:10.1144/0061047.

474 Reston, T. J., Pennell, J., Stubenrauch, A., Walker, I. & Pérez-Gussinyé, M. 2001.  
475 Detachment faulting, mantle serpentinization, and serpentinite-mud volcanism beneath the Porcupine  
476 Basin, southwest of Ireland. *Geology*, **29**(7), 587-590, doi:10.1130/0091-7613(2001)  
477 029<0587:DFMSAS>2.0.CO;2.

478 Reston, T. J., Gaw, V., Pennell, J., Klaeschen, D., Stubenrauch, A. & Walker, I. 2004.  
479 Extreme crustal thinning in the south Porcupine Basin and the nature of the Porcupine Median High:

480 implications for the formation of non-volcanic rifted margins. *Journal of the Geological Society*,  
481 **161**(5), 783-798, doi:10.1144/0016-764903-036.

482 Ryan, W.B., Carbotte, S.M., Coplan, J.O., O'Hara, S., Melkonian, A., Arko, R., Weissel,  
483 R.A., Ferrini, V., Goodwillie, A., Nitsche, F. & Bonczkowski, J. 2009. Global multi-resolution  
484 topography synthesis. *Geochemistry, Geophysics, Geosystems*, **10**(3), doi:10.1029/2008GC002332.

485 Sallarès, V., Gailler, A., Gutscher, M. A., Graindorge, D., Bartolomé, R., Gracia, E., Díaz, J.,  
486 Dañobeitia, J.J. & Zitellini, N. 2011. Seismic evidence for the presence of Jurassic oceanic crust in the  
487 central Gulf of Cadiz (SW Iberian margin). *Earth and Planetary Science Letter*, **311**(1), 112-123,  
488 doi:10.1016/j.epsl.2011.09.003.

489 Shannon, P. M. 1991. The development of Irish offshore sedimentary basins. *Journal of the*  
490 *Geological Society*, **148**(1), 181-189, doi:10.1144/gsjgs.148.1.0181.

491 Stockwell, J. W. 1999. The CWP/SU: Seismic Un\*x package. *Computers & Geosciences*, **25**,  
492 415-419, doi:10.1016/S0098-3004(98)00145-9.

493 Tate, M. P., White, N. & Conroy, J.-J. 1993. Lithospheric extension and magmatism in the  
494 Porcupine Basin west of Ireland. *Journal of Geophysical Research - Solid Earth*, **98**, 13 905-13 923,  
495 doi:10.1029/93JB00890.

496 Tate, M. P. & Dobson, M. R. 1988. Syn-and post-rift igneous activity in the Porcupine  
497 Seabight Basin and adjacent continental margin W of Ireland. *Geological Society, London, Special*  
498 *Publications*, **39**(1), 309-334, doi:10.1144/GSL.SP.1988.039.01.28.

499 Wangen, M. 2010. *Physical principles of sedimentary basin analysis*. Cambridge University  
500 Press.

501 Welford, J.K., Shannon, P.M., O'Reilly, B.M. and Hall, J. 2012. Comparison of lithosphere  
502 structure across the Orphan Basin–Flemish Cap and Irish Atlantic conjugate continental margins from  
503 constrained 3D gravity inversions. *Journal of the Geological Society*, **169**(4), 405-420,  
504 doi:10.1144/0016-76492011-114.

505 Wessel, P. & Smith, W. H. 1998. New, improved version of Generic Mapping Tools released.  
506 *Eos, Transactions American Geophysical Union*, **79**, 579-579, doi:10.1029/98EO00426.

507 White, N., Tate, M. & Conroy, J. J. 1992. Lithospheric stretching in the Porcupine Basin,  
 508 west of Ireland. *Geological Society, London, Special Publications*, **62**(1), 327-331,  
 509 doi:10.1144/GSL.SP.1992.062.01.25.

510 White, N., Thompson, M. & Barwise, T. 2003. Understanding the thermal evolution of deep-  
 511 water continental margins. *Nature*, **426**, 334-343, doi:10.1038/nature02133.

512 Wrigley, R., Intawong, A. & Rodriguez, K. 2014. Ireland Atlantic Margin: a new era in a  
 513 frontier basin. *First Break*, **32**(12), 95-100.

514 Zelt, C. A., & Forsyth, D. A. 1994. Modeling wide-angle seismic data for crustal structure:  
 515 Southeastern Grenville Province. *Journal of Geophysical Research - Solid Earth*, **99**, 11687-11704,  
 516 doi:10.1029/93JB02764.

517 **TABLES**

518 **Table 1.** *Modelling statistics for the northern line.* The “refr” (refractions) and “refl” (reflections)  
 519 subscripts refer to the parts of dataset considered.

Step	Iteration*	N <sub>refr</sub> †	N <sub>refl</sub> †	t <sub>RMS-refr</sub> ‡	t <sub>RMS-refl</sub> ‡	t <sub>RMS-all</sub> ‡	$\chi^2_{refr}$ §	$\chi^2_{refl}$ §	$\chi^2_{all}$ §
1	4	654	1,050	32	31	32	1.18	0.22	0.58
2	9	978	886	25	32	28	0.82	0.13	0.49
3	9	2,399	3,445	20	38	32	0.48	0.25	0.35
4	9	4,410	4,124	17	29	23	0.29	0.12	0.21
5	9	5,955	1,819	36	83	51	0.98	1.04	0.99
6	4	15,580	3,004	58	95	65	0.60	1.11	0.69
7	4	17,348	3,004	61	84	65	0.62	0.91	0.66

520 \*Iteration chosen to build the input model of next step (or final model for step 7).

521 †Numbers of picks used for the modelling.

522 ‡Root mean squared travel-time residuals, in milliseconds.

523 §Normalised chi-squared.

524 **Table 2.** *Modelling statistics for the southern line.* The “refr” (refractions) and “refl” (reflections)  
 525 subscripts refer to the parts of dataset considered.

Step	Iteration*	$N_{\text{refr}}\dagger$	$N_{\text{refl}}\dagger$	$t_{\text{RMS-refr}}\ddagger$	$t_{\text{RMS-refl}}\ddagger$	$t_{\text{RMS-all}}\ddagger$	$\chi^2_{\text{refr}}\S$	$\chi^2_{\text{refl}}\S$	$\chi^2_{\text{all}}\S$
1	4	1,952	2,149	15	30	24	0.56	0.59	0.58
2	3	4,685	5,491	19	27	24	0.44	0.29	0.36
3	5	8,163	3,638	38	58	45	0.51	0.67	0.56
4	4	15,502	8,563	47	70	56	0.48	0.89	0.63
5	4	23,520	13,209	54	86	67	0.43	0.87	0.59
6	2	29,927	13,209	69	84	74	0.59	0.84	0.67

526 \*Iteration chosen to build the input model of next step (or final model for step 6).

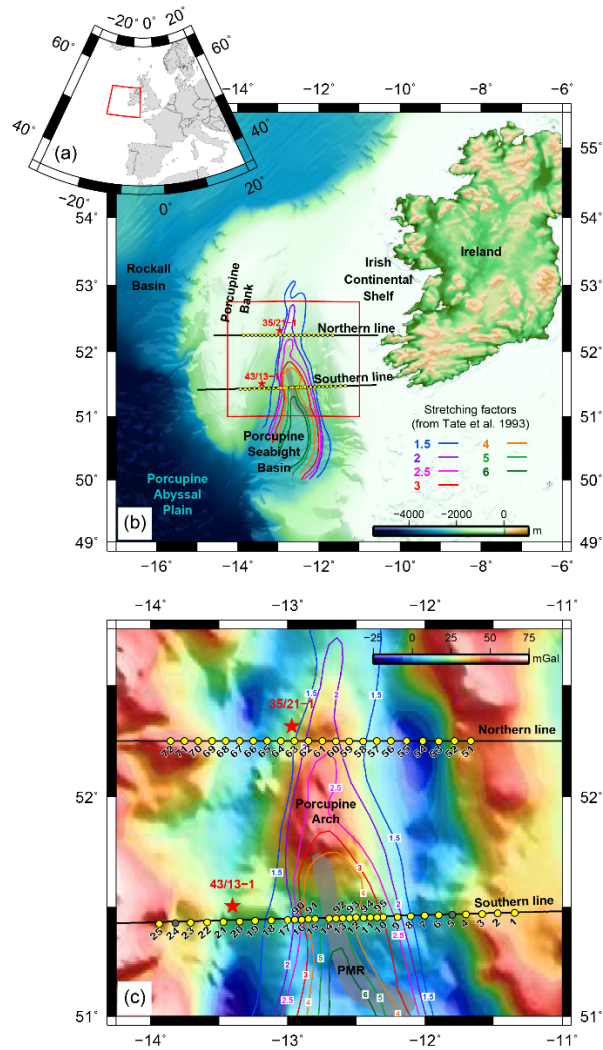
527 †Numbers of picks used for the modelling.

528 ‡Root mean squared travel-time residuals, in milliseconds.

529 §Normalised chi-squared.

530 **FIGURES**

531



532

533 **Fig. 1.** Location map.

534 (a) Location of the study area relative to Western Europe. (b) Bathymetric map of the study area

535 showing location of the two refraction profiles presented. Black lines show the location of the shots

536 along the northern and southern profiles. Bathymetry and elevation data are from [Ryan et al. \(2009\)](#).

537 Yellow circles show the positions of the ocean bottom instruments, which recorded the data used for

538 the seismic refraction processing. Grey circles are the instruments that failed to record usable data.

539 The coloured lines and the grey zone in the centre of the basin correspond to the values of stretching

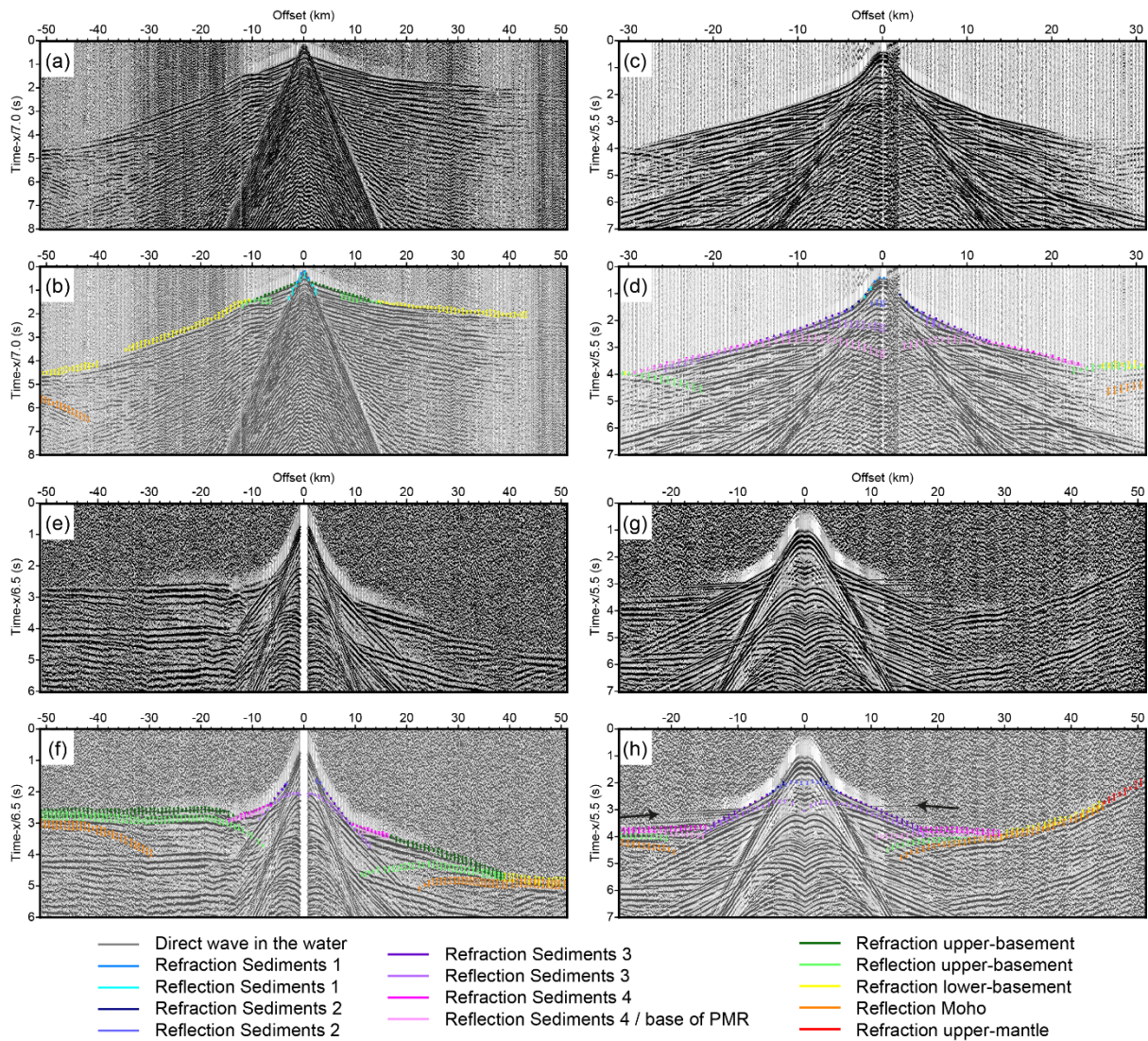
540 factors estimated from subsidence analysis and the location of the Porcupine Median Ridge (PMR),

541 respectively, from [Tate et al. \(1993\)](#). The red box shows the location of the map in part (c). The red

542 stars show the location of the wells presented in [Fig. 5](#). (c) Detailed gravity map around the two

543 profiles presented in this study. Colour and symbol codes are the same as for part (b). Black numbers

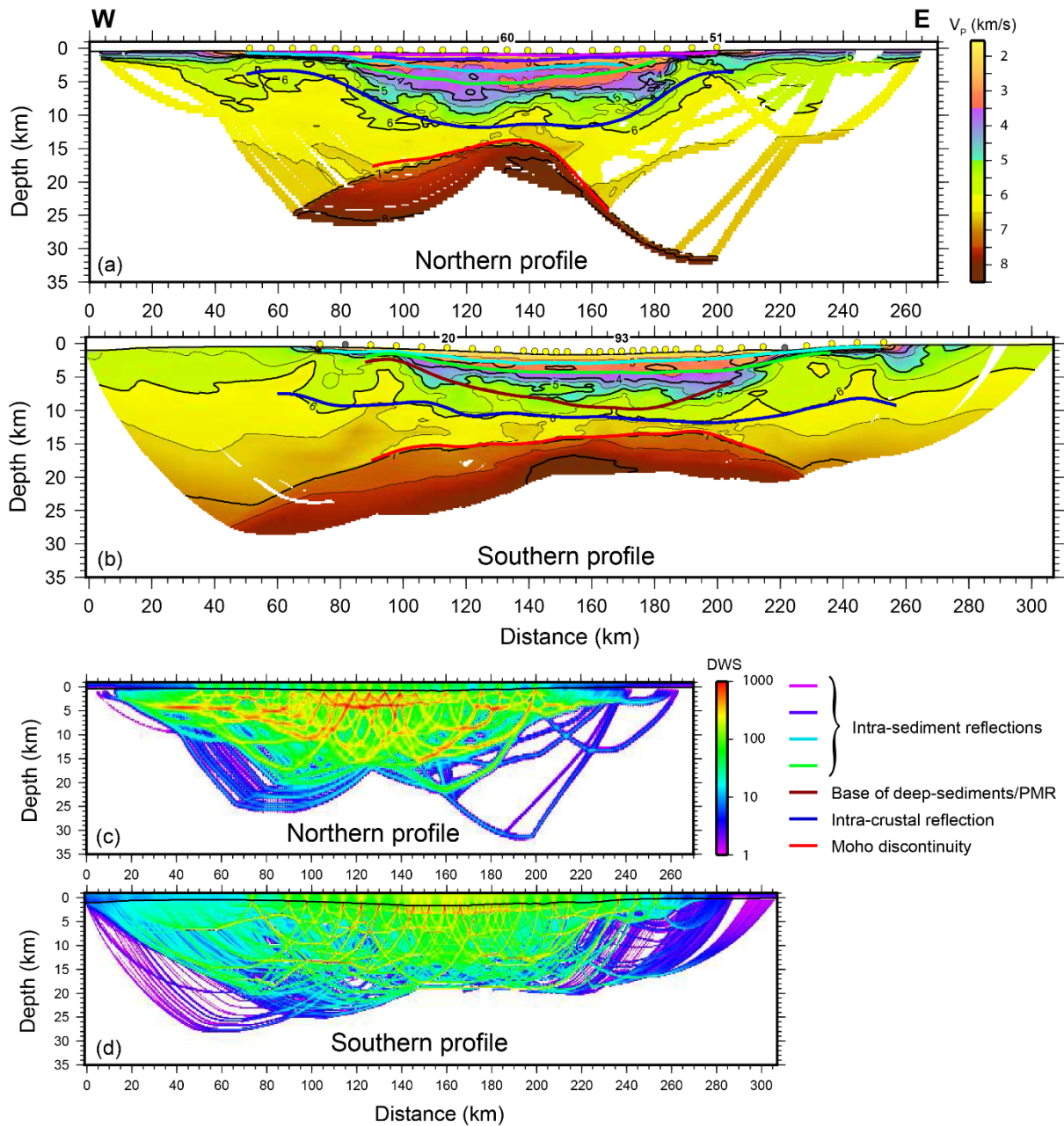
544 refer to the instrument numbers.



545

546 **Fig. 2.** Examples of data and phase picking.

547 Data were deconvolved and filtered for display. Colour bars represent the picks; colour codes are  
 548 detailed at the bottom of the figure. The height of each pick corresponds to its uncertainty. Every sixth  
 549 pick is shown. Black arrows show arrivals from a high-velocity layer that we chose to ignore for the  
 550 tomography modelling. (a) OBS 51, vertical geophone, along the northern line. (b) Same as (a) with  
 551 picks. (c) OBS 60, vertical geophone, along the northern line. (d) Same as (c) with picks. (e) OBH 20  
 552 along the southern line. (f) Same as (e) with picks. (g) OBH 93 along the southern line. (h) Same as  
 553 (g) with picks. Different reduction velocities were used for each plot; these are specified in the label  
 554 of the reduced time axis.



555

556 **Fig. 3.** Velocity models and derivative weight sums for the two profiles.

557 (a) Velocity model obtained after layer-stripping tomography modelling along the northern line.

558 Coloured interfaces show the interfaces used for the layered modelling, where they are illuminated by

559 wide-angle reflections. Colour codes are detailed in the lower right corner of the figure. Numbers

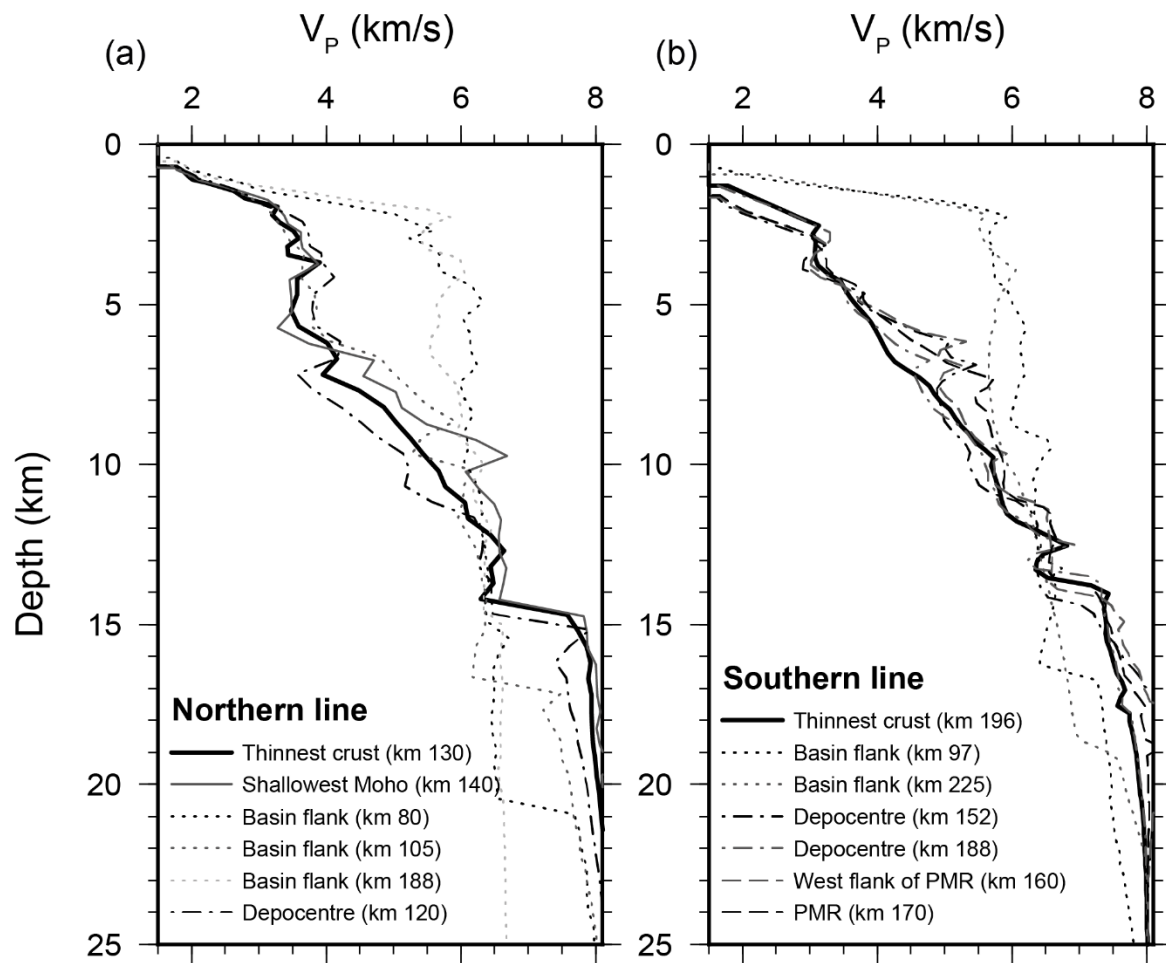
560 above instruments indicate the location of the instruments shown in Fig. 2. (b) Velocity model for the

561 southern profile. Colour codes are the same as for part (a) of this figure. (c) Derivative Weight Sum

562 (DWS) for the northern profile. High DWS indicates regions with dense ray coverage, i.e. regions

563 with the best velocity resolution. (d) DWS for the southern profile.



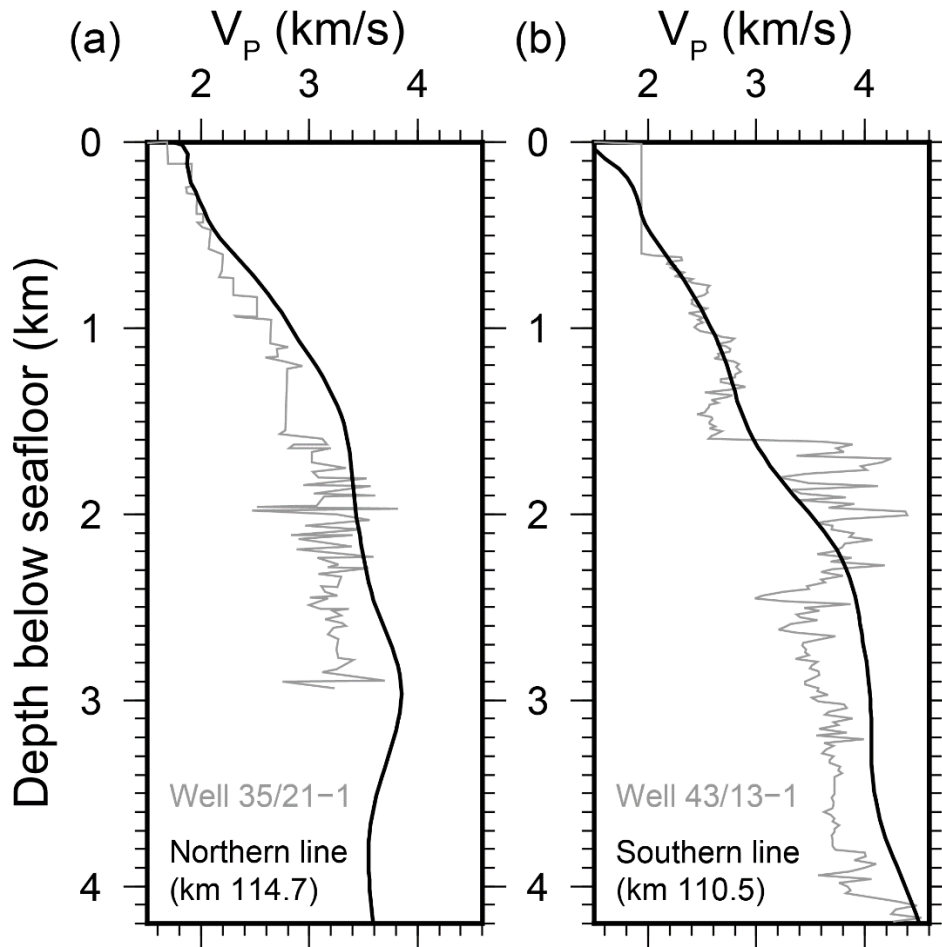


564

565 **Fig. 4.** Selection of vertical velocity profiles.

566 (a) Northern line. (b) Southern line.

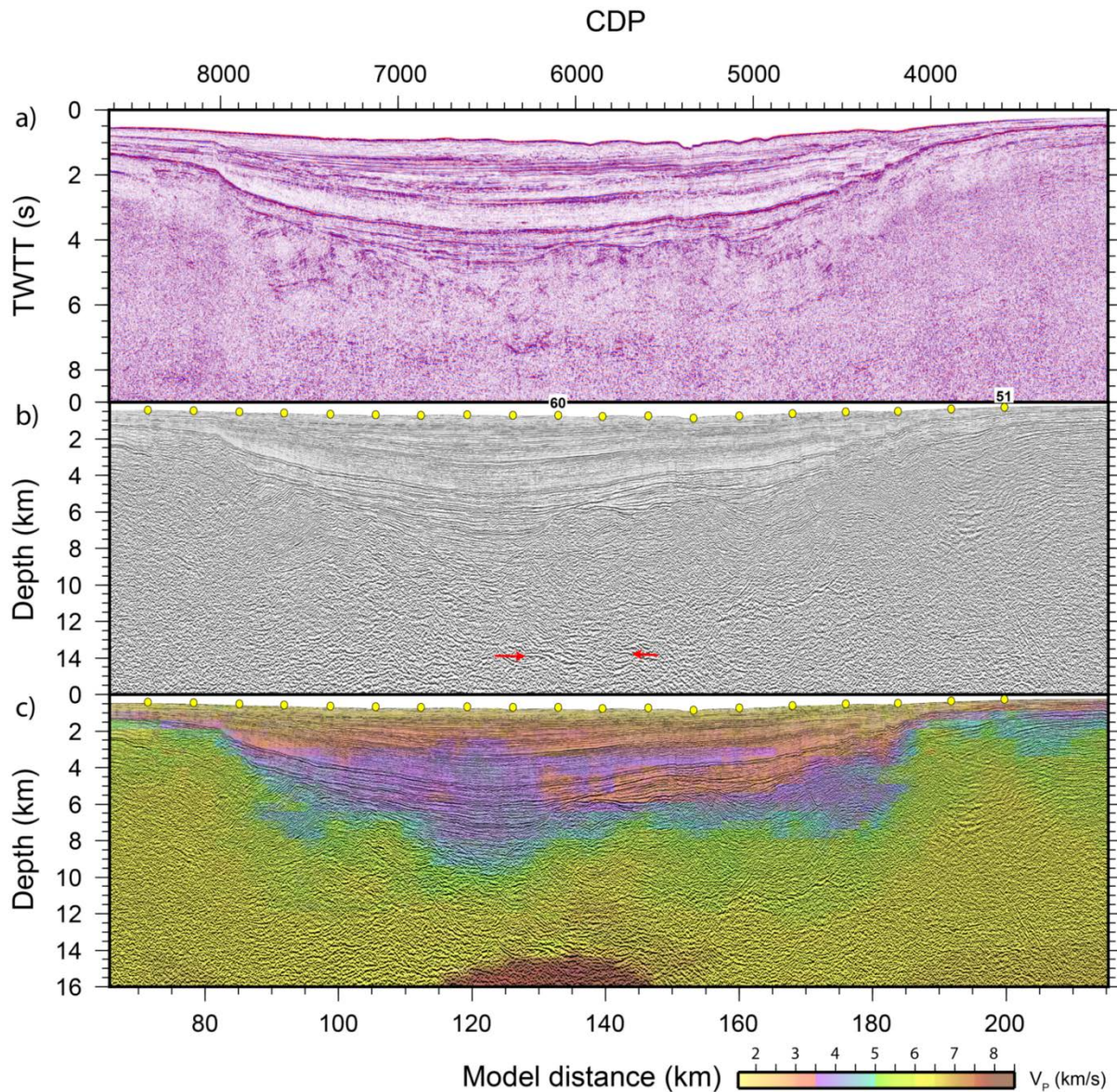
567



568

569 **Fig. 5.** Comparisons between P-wave velocities and nearby sonic logs from wells calibrated by check-  
 570 shot data.

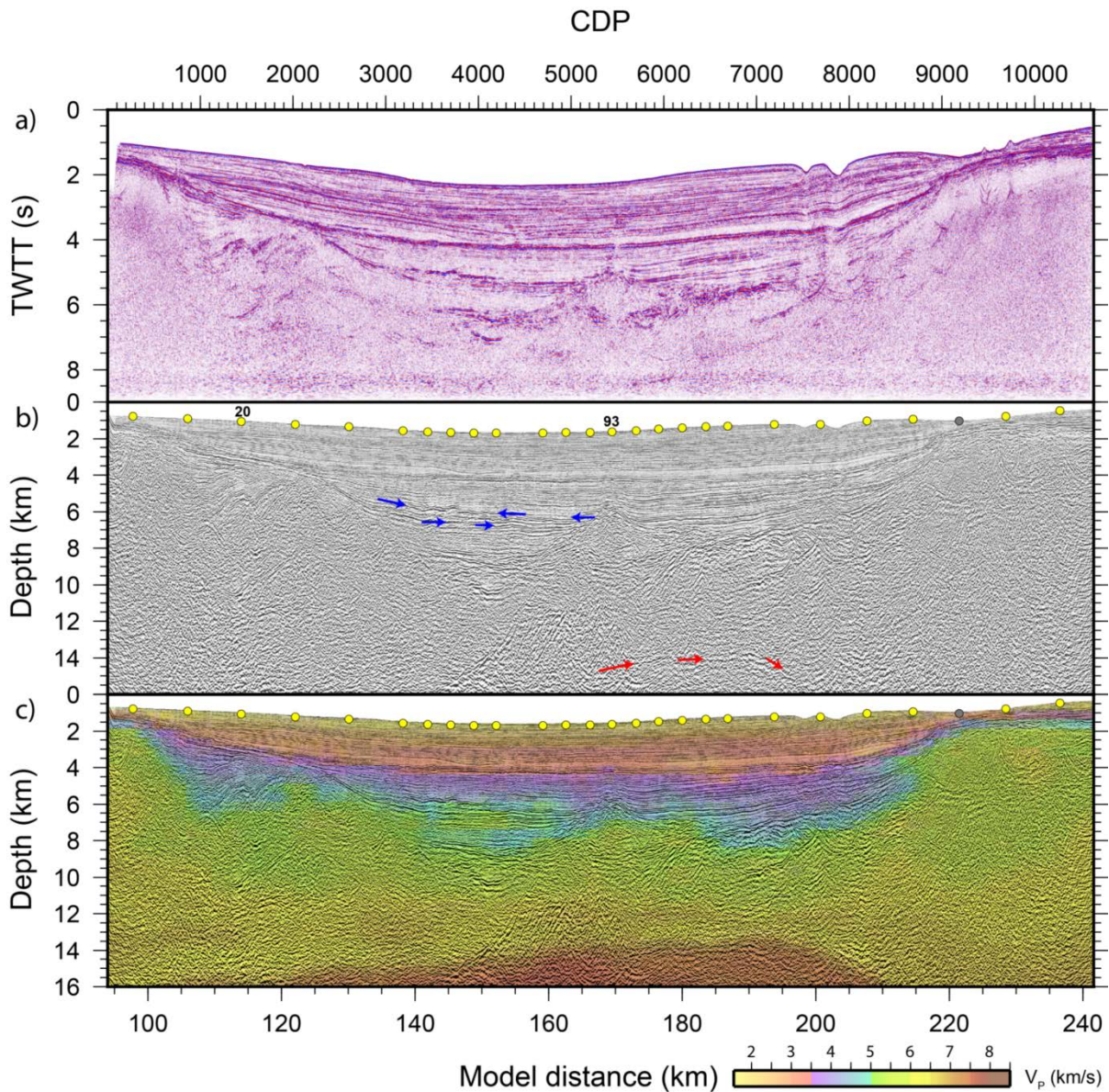
571 Borehole velocities were digitised from analogue records. (a) Northern line. (b) Southern line. No  
 572 data were acquired in the first 600 m. below seafloor.



573

574 **Fig. 6.** Comparison between velocity model of the Northern profile and coincident seismic reflection  
 575 data.

576 (a) Time migrated section of Wire 2 profile (Croker & Klemperer 1989). (b) Pre-stack depth migrated  
 577 section of Wire 2. Red arrows highlight deep reflectors, interpreted as Moho reflections. Numbers  
 578 above instruments indicate the location of the instruments shown in Fig. 2. (c) Superposition of the  
 579 results for the Northern profile on Wire 2.



580

581 **Fig. 7.** Comparison between velocity model of the Southern profile and coincident seismic reflection  
 582 data.

583 (a) Time migrated section of SPB97-115. (b) Pre-stack depth migrated section of SPB97-115. Blue  
 584 arrows indicate a highly reflective layer, interpreted as igneous. Red arrows highlight deep reflectors,  
 585 interpreted as Moho reflections. Numbers above instruments indicate the location of the instruments  
 586 shown in Fig. 2. (c) Superposition of the results for the Southern profile on SPB97-115.